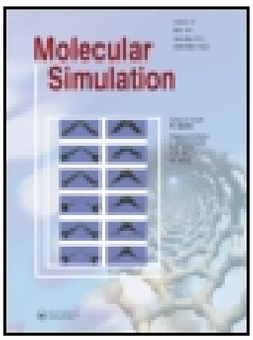

Molecular Simulation

ISSN: (Print) (Online) Journal homepage: https://www.tandfonline.com/loi/gmos20

Modelling aggregates of cetyltrimethylammonium bromide on gold surfaces using dissipative particle dynamics simulations

Yawei Liu, Jiachen Wei, Daan Frenkel & Asaph Widmer-Cooper

To cite this article: Yawei Liu, Jiachen Wei, Daan Frenkel & Asaph Widmer-Cooper (2021): Modelling aggregates of cetyltrimethylammonium bromide on gold surfaces using dissipative particle dynamics simulations, Molecular Simulation, DOI: 10.1080/08927022.2021.1948546

To link to this article: https://doi.org/10.1080/08927022.2021.1948546

MOLECULAR SIMULATION
https://doi.org/10.1080/08927022.2021.1948546

Taylor & Francis
Taylor & Francis Group

Modelling aggregates of cetyltrimethylammonium bromide on gold surfaces using dissipative particle dynamics simulations

Yawei Liu [a], Jiachen Wei [b,c], Daan Frenkel [d] and Asaph Widmer-Cooper [a,e]

[a]ARC Centre of Excellence in Exciton Science, School of Chemistry, University of Sydney, Sydney, Australia; [b]State Key Laboratory of Nonlinear Mechanics and Beijing Key Laboratory of Engineered Construction and Mechanobiology, Institute of Mechanics, Chinese Academy of Sciences, Beijing, People's Republic of China; [c]Shenzhen Bay Laboratory, Shenzhen, China; [d]Department of Chemistry, University of Cambridge, Cambridge, UK; [e]The University of Sydney Nano Institute, University of Sydney, Sydney, Australia

ABSTRACT

In this study, we developed a coarse-grained model based on the dissipative particle dynamics (DPD) method to investigate the aggregates of the cetyltrimethylammonium bromide (CTAB) molecules on gold surfaces including nanoparticles. We adopted the DPD model for CTAB solutions developed by Mao et al. [Modeling aggregation of ionic surfactants using a smeared charge approximation in dissipative particle dynamics simulations. J Phys Chem B. 2015;119:11673–11683] and introduced an attractive interaction between gold (Au) particles and bromide (Br^-) ions (i.e. Au-Br^- attraction) to bind CTAB molecules onto the gold surface via the electrostatic interactions between their cationic head groups and Br^- ions adsorbed on the gold surface. The proposed model with a proper Au-Br^- attraction can semi-quantitatively describe the structures of CTAB aggregates on a flat gold surface and around gold nanorods (AuNRs). As the Au-Br^- attraction and the CTAB concentration increase, the CTAB aggregates on the gold surface can change from micelles to a compact bilayer structure. In particular, our model predicts that in the CTAB layer, the inner sub-layer may have a higher ligand density than the outer sub-layer. The anisotropic distribution of CTAB molecules around AuNRs is also captured in our model.

ARTICLE HISTORY
Received 20 April 2021
Accepted 17 June 2021

KEYWORDS
Gold nanorod; cetyltrimethylammonium bromide; dissipative particle dynamics; ligand; bilayer

1. Introduction

Gold nanorods (AuNRs) [1–3] have become one of the most widely used platforms for developing new techniques in diverse fields such as chemical sensing and imaging [4], photothermal therapy [5], solar cells [6], display technologies [7], drug delivery [8] because of their unique and anisotropic physical properties [9, 10]. These extensive studies have benefited from the development of facile seeded growth synthesis, which provides a simple, convenient wet chemistry route to these nanomaterials [11–15]. This synthesis is accomplished by the controlled reduction of a gold salt onto pre-prepared Au seeds in the presence of cetyltrimethylammonium bromide (CTAB) surfactants and small amounts of silver ions from $AgNO_3$. CTAB is a bromine-containing cationic surfactant and assembles on the gold surface where it directs the growth of AuNRs and stabilises them after synthesis.

Since CTAB is crucial for anisotropic growth during synthesis and for the final stability of AuNRs in solution, plenty of experiments have been done to characterise the structure and distribution of CTAB on the gold surface. Early experiments [16–18] indicated that CTAB molecules form a bilayer structure around the gold nanoparticle in which the inner layer is bound to the gold surface via the head groups and the outer layer has the head groups facing the aqueous media, with a ligand surface density of 0.8−1.8 (molecules) nm^{-2} (per sub-layer on average) in 1−10 mM CTAB solutions. Direct measurement of the thickness (h) of the CTAB layer around AuNRs gave h=3.0−3.4 nm, which is smaller than twice the extended CTAB chain length (~4.34 nm), suggesting significant tilting or interdigitation of CTAB molecules on the gold surface [19]. A recent experimental analysis in 2019 found that the distribution of CTAB molecules on a AuNRs is anisotropic, with a 30% decrease in ligand density at the ends [20].

Meanwhile, a number of studies using atomistic molecular dynamic (MD) simulations have been done to explore the origin of the CTAB-induced anisotropic growth of AuNRs during seeded growth synthesis. In 2013, Meena and Sulpozi simulated CTAB molecules on different facets of gold nanoparticles and found that CTAB forms adjacent cylindrical micelles [21]. They also found that CTAB molecules preferentially cover the [100] and [110] facets, leaving the [111] facets at the ends of AuNRs more exposed. These results were further confirmed in their 2016 work [22]. It is now widely believed that this facet-dependent adsorption of CTAB molecules forces Au seeds to grow into rod-shaped particles. Recently, a simulation work from Silva et al. in 2020 verified that on a curved surface, a lower CTAB density and larger inter-micellar channels are generated compared to those on a flat surface, which can also contribute to the anisotropic growth of AuNRs [23].

In 2016, another study of Meena et al. provided evidence that Br^- ions act as the driving force for the adsorption and stabilisation of CTAB micelles on the gold surface, suggesting that the CTAB molecules are bound onto the surface via the electrostatic interactions between the cationic head groups

CONTACT Asaph Widmer-Cooper asaph.widmer-cooper@sydney.edu.au

and anionic sites which could be Br^- ions adsorbed on the gold surface [24].

All of the simulations described above found that the CTAB molecules are organised on all facets of the gold nanoparticle as a series of micelles, which is contradictory to the experimental results of the existence of the bilayer structure. In 2018, Silva and Meneghetti simulated CTAB assemblies on gold with different numbers of Br^- ions on the surface in their initial configurations, and found that as more Br^- ions are adsorbed on the gold surface, the CTAB aggregates can change from micelles to a compact CTAB bilayer [25].

Atomistic MD simulations provide a useful way to understand the interaction of CTAB molecules with the gold surface at the molecular level. However, this simulation approach is too expensive to investigate the behaviour of AuNRs at the nanoparticle-level, such as the rod dynamics during self-assembly [26–28] or during phoretic motions [29–32]. The only feasible way under the limit of computational resources is to perform simulations based on a coarse-grained description of components in the system [33–36]. For example, we have recently developed a coarse-grained model based on the dissipative particle dynamics (DPD) method to explain the oriented assembly of AuNRs in the presence of an electric field [32]. In that DPD model, the details of the ligands (the experiments used CTAB-stabilised AuNRs wrapped by polyelectrolytes to maintain a stable highly-charged surface) were completely ignored, and the surface charges were simply represented by regularly distributed point charges fixed on the surface of the nanorods. That DPD model is, therefore, unable to describe important properties related to the CTAB ligands, including deformation of the CTAB layer, the micellar/bilayer structure, and the ion distribution near the CTAB layer. A coarse-grained model with CTAB molecules explicitly considered is also necessary for studying processes that directly utilise CTAB molecules on the gold surface such as drug delivery [2, 8].

In this study, we developed a coarse-grained model based on the DPD method that can be used to study the assembly of CTAB on gold surfaces. This model can semi-quantitatively reproduce the results of previous experiments and atomistic MD simulations related to the organisation of CTAB molecules around gold nanoparticles. We expect that it will prove useful in future work for understanding the effect of the CTAB layer on the self-assembly and phoretic motion of AuNRs.

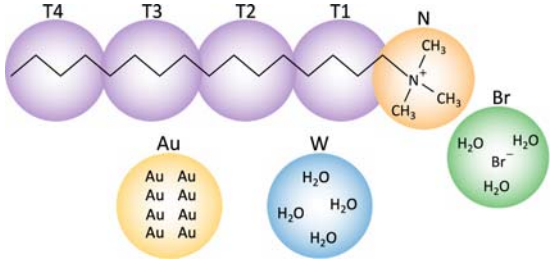

Figure 1. (Colour online) Schematic illustration of the coarse-grained models for CTAB and other components in the system. Each CTA^+ chain is represented by one N bead for the hydrophilic cationic head group and four T beads (i.e. T1-T4) for the hydrophobic tail. Water and Br^- ions are modelled by W and Br beads, respectively, with one bead consisting of 4 water molecules or 1 ion plus 3 water molecules. Solid gold is made up of Au beads with one bead representing ~8 gold atoms.

The paper is organised as follows: In Section 2, we introduce our model and simulation method. We then use this model to study the assembly of CTAB on a flat gold surface and around a AuNR, with the results presented in Section 3. A brief summary of the key results is given in Section 4.

2. Model and method

2.1. Model

We adopted the DPD model developed by Mao et al. in Ref. [37] for the CTAB solutions. This model can faithfully describe the bulk aggregation of CTAB molecules over a wide range of CTAB and ion concentrations. As shown in Figure 1, one CTA^+ chain is modelled as one N bead representing the hydrophilic cationic head group plus four T beads (i.e. T1-T4) representing the hydrophobic tail. These N and T beads are connected by either harmonic or FENE [38] bonds with the force between beads i and j

$$\mathbf{F}_{ij}^B = k_b \frac{(r_0 - r_{ij})}{1 - (r_{ij} - r_0)^2 / r_m^2} \hat{\mathbf{r}}_{ij}, \tag{1}$$

where $r_{ij} = |\mathbf{r}_{ij}|$ is the centre-to-centre distance between the two beads, $\hat{\mathbf{r}}_{ij} = \mathbf{r}_{ij}/r_{ij}$ is the unit vector connecting the two beads, k_b is the bond strength constant, r_0 is the equilibrium bond length and r_m is the maximum extent of the bond. In addition to the nearest neighbour (1–2) bonds, the second neighbour (1–3) harmonic or FENE bonds are used to control the flexibility of the chain. This approach without invoking angle and torsion potentials can reproduce the conformation obtained from atomistic simulations of CTAB molecules [37].

The water and Br^- ions are modelled as W and Br beads, respectively, with one bead representing 4 water molecules or 1 ion plus 3 water molecules (i.e. the coarse-graining level $N_m = 4$) (see Figure 1).

Solid gold is simply modelled as a rigid body of many 'frozen' DPD Au beads arranged in an FCC lattice with the number density of $3r_c^{-3}$ (i.e. the common density in DPD simulations) where r_c is the diameter of the beads. This means each Au bead approximately contains 8 gold atoms.

All DPD beads (i.e. N, T, W, Br and Au beads) interact with each other via a conservative force $\mathbf{F}_{ij}^C$, a dissipative force $\mathbf{F}_{ij}^D$ and a random force $\mathbf{F}_{ij}^R$ given by

$$\begin{aligned} \mathbf{F}_{ij}^C &= a(1 - r_{ij}/r_c)\hat{\mathbf{r}}_{ij} && r_{ij} < r_c \\ \mathbf{F}_{ij}^D &= -\gamma(1 - r_{ij}/r_c)^2(\hat{\mathbf{r}}_{ij} \cdot \mathbf{v}_{ij})\hat{\mathbf{r}}_{ij} && r_{ij} < r_c \\ \mathbf{F}_{ij}^R &= \sqrt{2k_B T\gamma}(1 - r_{ij}/r_c)\theta_{ij}\Delta t^{-1/2}\hat{\mathbf{r}}_{ij} && r_{ij} < r_c \end{aligned} \tag{2}$$

between beads i and j [39, 40]. Here, a is the conservative force constant, γ is the dissipative constant, $\mathbf{v}_{ij}$ is the vector difference in velocities between the two beads, θ_{ij} is a Gaussian white noise variable with $\theta_{ij} = \theta_{ji}$, and Δt is the simulation time step. All these three forces vanish when $r_{ij} \geq r_c$.

The electrostatic interaction between charged beads (i.e. N and Br beads) is described by the smeared-charge Coulomb

potential with the Slater-type charge density distribution $\rho(r) = (q/\pi\lambda^3)\exp(-2r/\lambda)$ where λ is the effective smearing length and q is the charge of one bead [41]. The electrostatic force between charged beads i and j is then given by

$$\mathbf{F}_{ij}^{E} = \frac{\Gamma z_i z_j}{4\pi r_{ij}^2}\left[1 - \exp\left(\frac{-2r_{ij}}{\lambda}\right)\left(1 + \frac{2r_{ij}}{\lambda}(1 + \frac{r_{ij}}{\lambda})\right)\right]\hat{\mathbf{r}}_{ij}, \quad (3)$$

where Γ is the permittivity coupling parameter defined as $\Gamma = e^2/\epsilon_0\epsilon_r$, in which e is the electron charge, ϵ_0 is the dielectric constant for vacuum, and ϵ_r is the relative permittivity of the medium, z_i (z_j) is the valence of bead i (bead j) defined by $z = q/e$.

In order to mimic the binding mechanism of CTAB molecules on the gold surface observed in atomistic MD simulations [24], instead of applying an attraction between N and Au beads, we introduced attractive forces between Br and Au beads so that CTA^+ chains can be indirectly bound onto the gold surface via the electrostatic interactions between the N (i.e. the head groups of CTA^+ chains) and Br (i.e. Br^- ions) beads adsorbed on the gold surface. This additional attractive force is given by a truncated Morse potential,

$$\mathbf{F}_{ij}^{\text{Morse}} = -2D_0\alpha r_{ij}\left(1 - e^{-\alpha(r-r_0)}\right)e^{-\alpha(r-r_0)} \quad (4)$$

and truncated at $r = 1.5r_c$, with D_0 the force constant, r_0 the equilibrium distance, and α the parameter for the range of the force. Note that in our model, this Morse force is only applied between Au beads on the gold surface and Br beads.

2.2. Simulation method

In our simulations, all quantities were scaled by the mass unit m_W (i.e. the W bead mass), the length unit r_c, the energy unit k_BT, the time unit $\tau = r_c\sqrt{m_W/(k_BT)}$, and the charge unit e. Hence, $r_c^* = m_W^* = (k_BT)^* = \tau^* = e^* = 1$. The superscript asterisk means the quantity is in reduced units. The reduced units can be converted to real units using the following relations: $r_c = 0.71$ nm, $m_w = 1.2 \times 10^{-25}$ kg, $k_BT = 4.1 \times 10^{-21}$ J, $\tau = 4$ ps and $e = 1.6 \times 10^{-19}$ C. Converting units, the DPD solvent at a reduced number density $\rho^* = 3$ can approximately reproduce the thermodynamic properties of bulk water.

For simplicity, all fluid beads (i.e. N, T, W, and Br beads) have the same mass (i.e. $m_C = m_A = m_N = m_T = m_W$), and Au beads have $m_{Au} = 20m_W$. For DPD forces, we set $\gamma^* = 100$. For Morse forces, we set $\alpha^* = 2$, $r_0^* = 0.7$. In this work, D_0 is treated as a variable, which controls the amount of Br beads adsorbed on the gold surface, and is explored to find a reasonable range to ensure that the properties of CTAB molecules on the gold surface can be well captured by our model. For charged beads, z=1 for N beads, z=−1 for Br beads, and $\Gamma^* = e^2/(\epsilon_0\epsilon_r k_B T r_c) = 12.65$ (corresponding to $\epsilon_r = 78.3$ for water at $T = 25°C$). Other parameters for the forces in Equations 1 and 2 are given in Tables 1 and 2, respectively.

Figure 2 gives two examples of the simulation boxes used to examine the capabilities of our DPD models for studying CTAB molecules on a flat gold surface and around a AuNR, respectively. Quasi-2D simulation boxes were employed in all simulations to reduce the computational costs in this work.

Table 1. Parameters for bond forces (Equation (1)) [37].

bead pairs	k_b [k_BT/r_c^2]	r_0 [r_c]	r_m [r_c]
T-T	280	0.605	2.0
T1-N	200	0.4	∞
T-(T)-T	20	1.5	4.0
T2-(T1)-N	150	1.3	∞

Table 2. Parameters for DPD forces (Equation (2)).

bead pairs	a [k_BT/r_c]
W/Br/N-W/Br/N	106.5 [37]
W/Br-T	129.9 [37]
N-T	111.5 [37]
W/Br/N-Au	106.5
T-Au	129.9

Notes: To prevent the fluid beads permeating into the gold, we only use the DPD forces in this table for the Au beads on the gold surface. Other inner Au beads have strong DPD repulsive forces of $a = 400k_BT/r_c$ with other fluid beads.

In the simulations of CTAB molecules on a flat gold surface (Figure 2 (a)), the size of the quasi-2D box $L_x = L_z \sim 23.5$ nm and $L_y \sim 6.3$ nm. All water/ion beads and CTAB molecules were confined between two parallel solid walls made of Au beads. In the initial configurations, all CTAB molecules were arranged in a bilayer structure near the bottom wall. During these simulations, all Au beads were frozen at their initial positions.

In the simulations of CTAB molecules around the AuNR (Figure 2(b)), the size of the quasi-2D box $L_x = L_z \sim 31.3$ nm and $L_y \sim 3.9$ nm. There was a quasi-2D AuNR consisting of a rectangular segment of length $L \sim 10.7$ nm and width $d \sim 3.6$ nm capped with two hemi-cylinders. In the initial configurations, all CTAB molecules were arranged in a bilayer structure around the AuNR. During these simulations, the AuNR was treated as a rigid body. This means that at each time-step, the total force and torque on the rigid AuNR was computed as the sum of the forces on its constituent Au beads. Note that during the simulations, we turned off the components of torque in x and z dimensions so the rigid AuNR only rotates along y axis, corresponding to an 'infinite' cylindrical AuNR in the periodic quasi-2D system (Figure 2(b)).

In all simulations, there were N_{CTA^+} CTA^+ chains in the box. N_{Br^-} Br beads and a suitable number of W beads were added to keep the system electrically neutral and the average number density of all beads $\rho^* = 3$.

All simulations were carried out using the parallel software package LAMMPS [42] in an isochoric, isothermal (NVT) ensemble. Periodic boundary conditions were applied in all directions. The velocity-Verlet algorithm was used to integrate the equations of motion with a time step $\Delta t^* = 0.002$. For the electrostatic interaction, at short range the interaction at $r_{ij}^* < 2.5$ was explicitly calculated by Equation (3) with $\lambda^* = 0.25$, while at long range the electrostatic interaction of smeared charges reduced to the Coulomb potential of point charges and the standard Ewald summation [43] was used to account for the periodic boundary conditions. Each

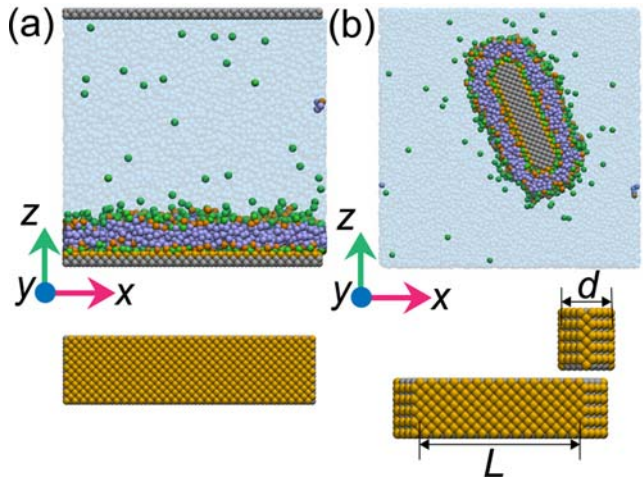

Figure 2. (Colour online) Two typical simulation boxes used in this work for simulating CTAB molecules (a) on a flat surface and (b) around a AuNR. Water beads are transparent blue, N beads are orange, T beads are purple, Br beads are green, Au beads on the surface that can attract Br beads are yellow and other Au beads are grey. Views of the gold [100] facet exposed to the aqueous media in (a) and the end/side surfaces of the AuNR in (b) are also given.

simulation was equilibrated for 0.5×10^7 steps with data from a further 1.0×10^7 steps used to calculate the equilibrium properties.

3. Results and discussions

3.1. CTAB molecules on flat gold surfaces

Figure 3 shows the snapshots of the equilibrium configurations obtained from the simulations with different values of N_{CTA^+} and D_0. Here, we assume that all CTA^+ chains are organised in a bilayer structure on the gold surface, and use the average ligand surface density per sub-layer (i.e. $\overline{\rho_s} = N_{CTA^+}/2A$ with $A = L_x L_y$ the area of the gold surface) to characterise the amount of CTAB molecules in the system. We also analysed the distributions of different components near the gold surface via their local densities as a function of the distance from the surface (i.e. ρ *vs.* z), and the actual ligand surface density of CTA^+ chains (ρ_s) through the accumulative ρ_s along z (i.e. $acc.\rho_s$ *vs.* z) calculated by integrating ρ of N beads. These calculated results are given in Figures 4 and 5.

Since the CTAB concentrations in all systems $>\sim 150$ mM and are much larger than the critical micelle concentration (i.e. ~0.9 mM in experiments [44] and ~2.6 mM in current DPD model [37]), we observed the aggregation of CTAB molecules in all simulations. The locations and structures of these CTAB aggregates depend on $\overline{\rho_s}$ (i.e. the adsorption amount) and D_0 (i.e. the binding strength).

At $D_0^* = 0.0$, CTAB aggregates can freely diffuse into the bulk solution in the systems with $\overline{\rho_s} \leq 2.0\ \mathrm{nm}^{-2}$ (see Figure 3(a ,f,k)).

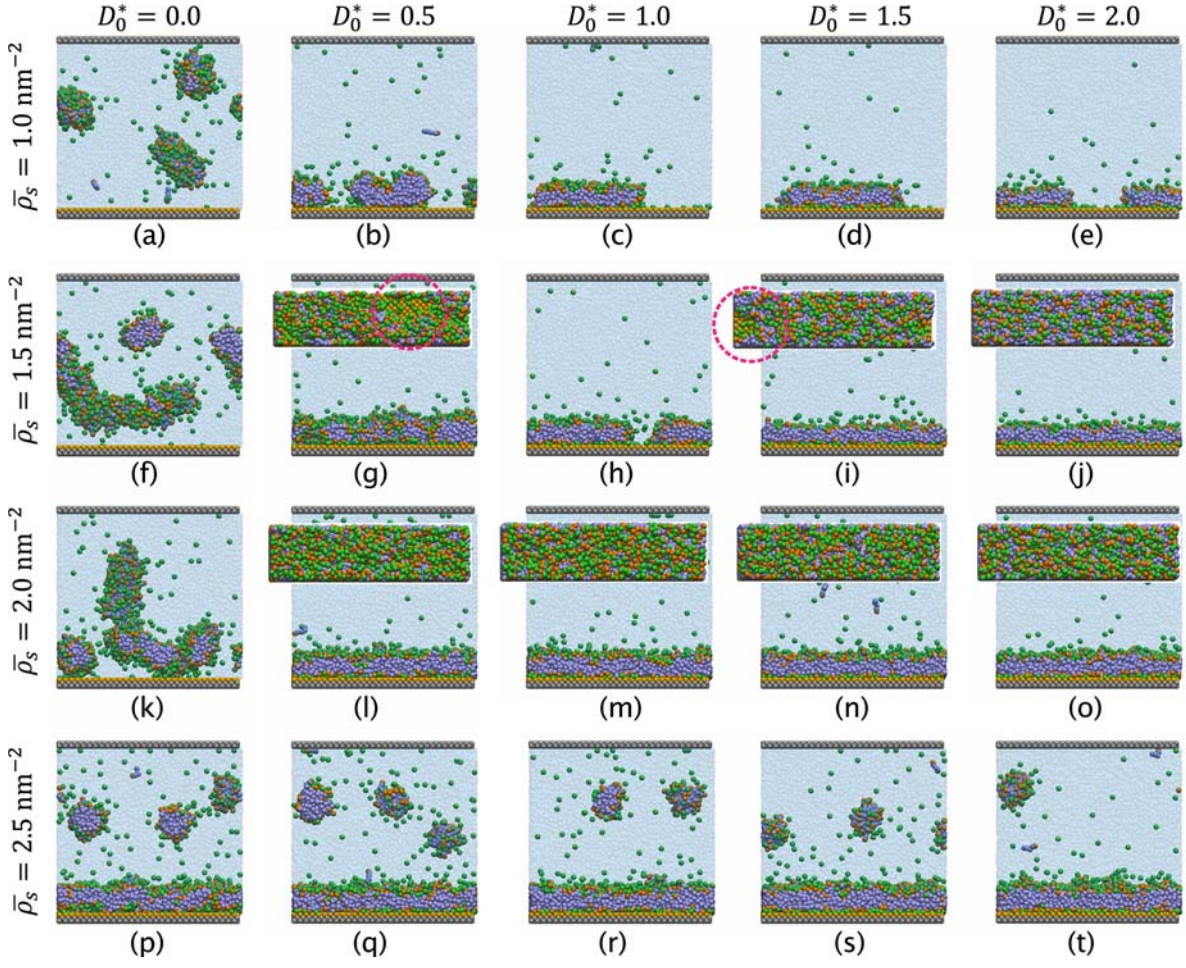

Figure 3. (Colour online) Snapshots of the equilibrium configurations for CTAB molecules on the flat [100] gold surface obtained from the simulations with different values of $\overline{\rho_s}$ and D_0. Top views are given in some sub-figures to show the coverage of CTAB molecules on the gold surface, and the red circles indicate the locations of exposed gold surface.

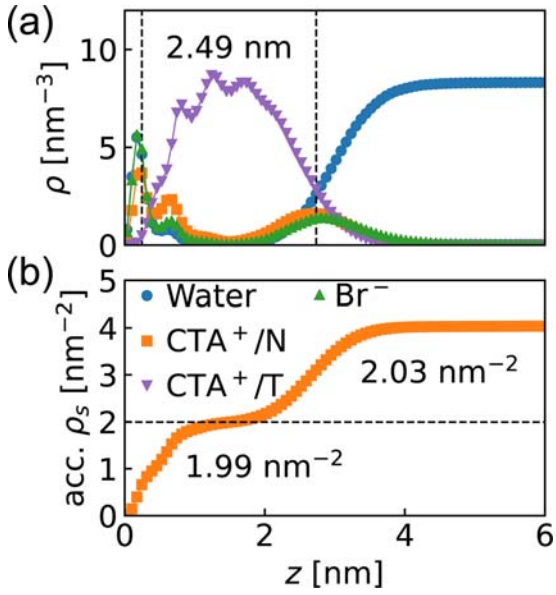

Figure 4. (Colour online) (a) The density profiles (i.e. ρ *vs.* z) of different components near the gold surface, and (b) the accumulative ρ_s along z (i.e. *acc.*~ρ_s *vs.* z) in the system with $\overline{\rho_s} = 2.5\,\mathrm{nm}^{-2}$ and $D_0^* = 0.0$ (see Figure 3 (p)). In (a), the two vertical dash lines indicate the positions (i.e. the distance from the gold surface) of the two main peaks appearing in the curve of the density distribution for *N* beads (i.e. the head of CTA^+ chains). The distance between these two lines, which defines the thickness of the CTAB layer [25], is also is given. In (b), the horizontal dash line indicates the boundary between the inner/outer sub-layers, and the ligand surface density in these two sub-layers are given.

In the system with $\overline{\rho_s} = 2.5\,\mathrm{nm}^{-2}$ (see Figure 3(p)), there are several small CTAB micelles forming in the bulk solution, and a large CTAB aggregate forming and staying on the gold surface during the whole simulation time. Replacing the bulk CATB micelles with the same amount of W beads and re-equilibrating the system, we observed a similar final configuration as shown in Figure 3(k), thus confirming that the electrostatic repulsions from the floating CATB micelles in the bulk force the large CATB aggregate to sit on the gold surface even there is no additional attraction from the gold surface. The density profiles near the gold surface in Figure 4(a) clearly show there are two main peaks in ρ *vs.* z of N beads (i.e. the head groups of CTA^+ chains) and a distinct hydrophobic region where W beads (i.e. water) are excluded, indicating the large CTAB aggregate on the gold surface has a bilayer structure. The configuration in Figure 3(p) corresponds to a saturated adsorption state when there is no additional attraction from the gold surface (i.e. $D_0^* = 0$) in our model, and thus provides an important reference for investigating the structures of CTAB molecules at other values of $\overline{\rho_s}$ and D_0. The two main density peaks of N beads in Figure 4(a) approximately indicate the thickness of the CTAB bilayer $h \sim 2.49$ nm, and the accumulative ligand surface density in Figure 4 (b) show there are nearly equal number of CTA^+ chains in each sub-layer, and $\rho_s \sim 2.0\,\mathrm{nm}^{-2}$.

At $D_0^* > 0$, Br beads can be adsorbed on the gold surface and so do the CTAB aggregates under the electrostatic attractions between N and Br beads. If the CTAB concentration is low (e.g. $\overline{\rho_s} = 1.0\,\mathrm{nm}^{-2}$ in Figure 3(b)–(e)), CTAB molecules aggregate in elongated micelles adsorbed on the gold surface. These micelles spread on the surface and thus become flatter as D_0^* increases, but there is always a large area of gold surface exposed to the aqueous solvent. With a higher CTAB concentration (e.g. $\overline{\rho_s} = 1.5\,\mathrm{nm}^{-2}$ in Figure 3(g)–(j)), most of the gold surface is covered by CTAB aggregates and there are some small channels in the CTAB layer connecting the aqueous solvent with the gold surface. These channels shrink as D_0^* increases and eventually disappear at $D_0^* = 2.0$ (see Figure 3 (j)) where a compact CTAB bilayer forms and covers the whole gold surface. Compact CTAB bilayers were always observed in the systems with a sufficient amount of CTAB molecules at $D_0^* = 0.5 - 2.0$ (e.g. $\overline{\rho_s} = 2.0$ and $2.5\,\mathrm{nm}^{-2}$ Figure 3 (l)–(o) and (q)–(t)). Moreover, in the systems with $\overline{\rho_s} = 2.5\,\mathrm{nm}^{-2}$, as D_0^* increases, less and less micelles form in bulk solution (see Figure 3(q)–(t)), indicating that the CTAB bilayer contains more CTA^+ chains at larger D_0^*.

We analysed the CTAB layer on the gold surface in the systems with $\overline{\rho_s} \geq 1.5\,\mathrm{nm}^{-2}$ and $D_0^* \geq 0.5$ in detail. From the plots of ρ *vs.* z in Figure 5, we can obtain that:

1 (i) As D_0^* increases, more Br beads are adsorbed on the gold surface, which provides a stronger electrostatic attraction to bind CTA^+ chains onto the surface and changes the structure of adsorbed CTAB aggregates.
2 (ii) The distribution of N beads shows two main peaks in ρ, and there is a third, smaller density peak near the main one at the gold surface when $D_0^* \leq 1.5$ (also see Figure 4 (a)). These features were also observed on the gold [100] facets in atomistic simulations, and the existence of the small peak was attributed to the weaker binding interactions for Br^- ions on these facets [25].
3 (iii) When $\overline{\rho_s} = 1.5\,\mathrm{nm}^{-2}$, the thickness of the CTAB layer (h), defined by the distance between the two main density peaks of N beads, is continuously decreasing as D_0^* increases, corresponding to the compacting of CTAB aggregates and shrinking/disappearing of channels observed from snapshots in Figure 3(g) –(j). When $\overline{\rho_s} = 2.0\,\mathrm{nm}^{-2}$, h almost remains constant at $D_0^* \leq 1.5$ and significantly reduces at $D_0^* = 2.0$, indicating that the CTAB bilayer is a compact structure which can remain a constant thickness unless the electrostatic attractions from the gold surface are too strong. When $\overline{\rho_s} = 2.5\,\mathrm{nm}^{-2}$, h remains at 2.49 nm at $D^* \leq 0.5$ (also see Figure 4(a)) and increases to 2.63 nm at $D_0^* = 1.0$ and 1.5 because more CTA^+ chains are adsorbed on the gold surface, and then slightly decreases to 2.56 nm at $D_0^* = 2.0$.
4 (iv) The values of h for the compact CTAB bilayers formed in our simulations (see Figure 3(l)–(t), Figure 4(a) and Figure 5) are smaller than the thickness of the compact CTAB bilayer on the gold surface measured in experiments (i.e. 3.0−3.4 nm [19]) and in atomistic simulations (i.e. ~3.4 nm [25]). This discrepancy is mainly because the length of CTA^+ chains (l) in the DPD model is dramatically underestimated due to the coarse-grinning operation. From the equilibrium bound lengths in Table 1, we obtained $l \sim 1.57$ nm, which is much smaller than the actual value (i.e. ~2.17 nm). If we take an offset of 0.71 nm (i.e. the diameter of one bead) into account, for CTAB bilayers

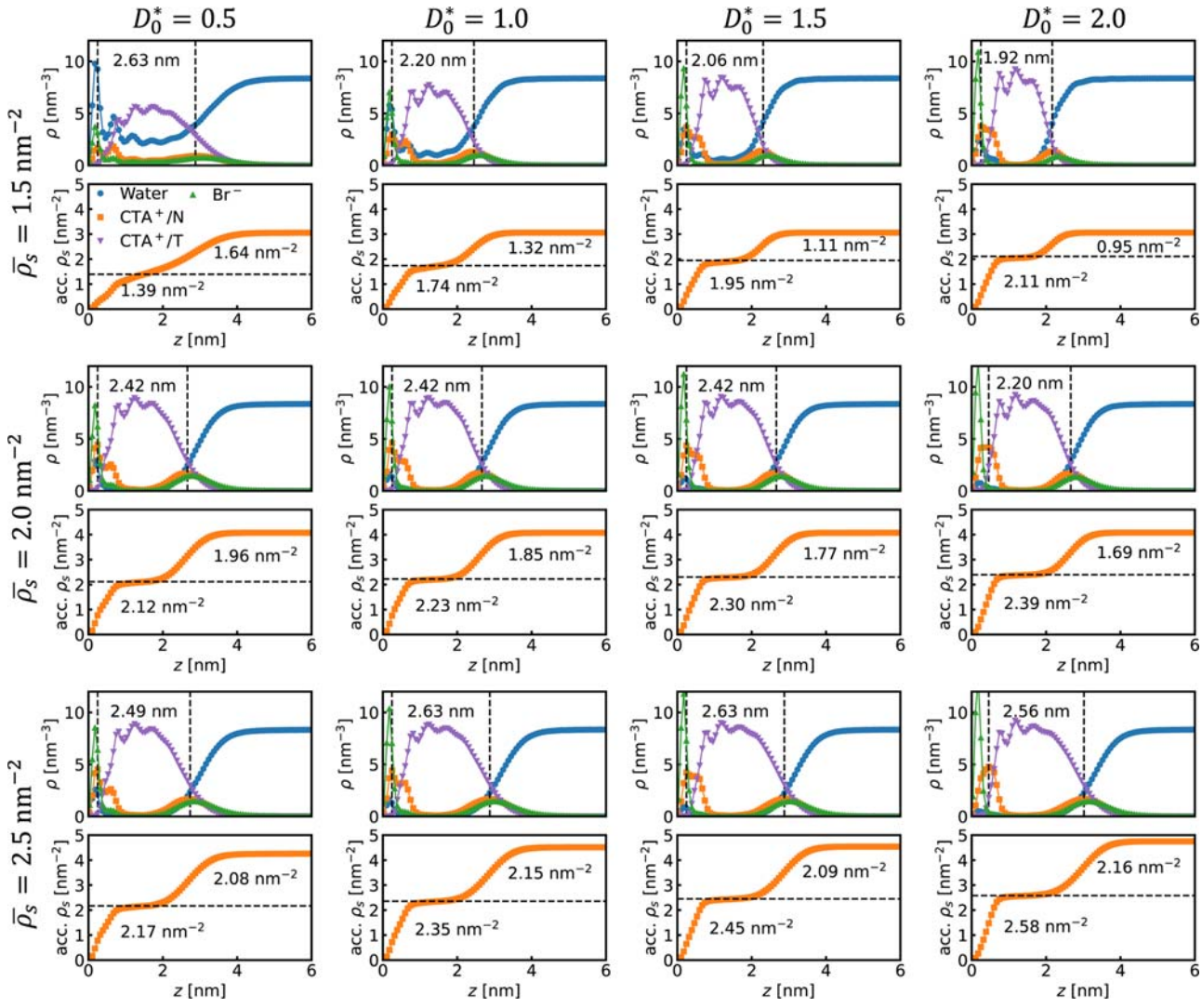

Figure 5. (Colour online) The density profiles (i.e. ρ *vs.* z) of different components near the flat gold surface, and (b) the accumulative ρ_s along z (i.e. $acc.\rho_s$ *vs.* z) in the system with different values of $\overline{\rho_s} \geq 1.5\ \mathrm{nm}^{-2}$ and $D_0^* \geq 0.5$. The thickness of the CTAB layer and the ligand surface density in the inner/outer sub-layers are given in the corresponding sub-figures.

at $D_0^* \leq 1.5$, the resulting $h \sim 3.1 - 3.3$ nm is very close to the experimental values. The thickness of CTAB bilayers at $\overline{\rho_s} = 2.0\ \mathrm{nm}^{-2}$ and $D_0^* = 2.0$ is still smaller than the experimental values even taking the offset into account, thus we suggest using a value of $D_0^* \leq 1.5$ in our model to ensure that the thickness of the CTAB bilayer is faithfully reproduced. Meanwhile, our results of h for compact CTAB bilayers in Figure 5 are always smaller than $2l \sim 3.14$ nm, supporting the partial interdigitation of CTA$^+$ chains in CTAB layers [19].

Table 3. Saturated average ligand surface density on the gold surface at different values of D_0.

D_0^*	$\rho_s^{\mathrm{satd.}}$ [nm^{-2}]
0.0	2.01
0.5	2.12
1.0	2.25
1.5	2.27
2.0	2.37

(v) The compact CTAB bilayers at $\overline{\rho_s} = 2.0$ and $2.5\ \mathrm{nm}^{-2}$ have a distinct hydrophobic region composed of tails of CTA$^+$ chains. The density profiles of T beads also suggest the tails are overlapping in these hydrophobic regions. In addition, near N beads in the outer layer, we can observe a diffuse distribution of Br beads at the 'soft' ligand-solvent interface, which is a very different from that in a more coarse-grained model where the charged AuNRs were simply modelled as hard rods with fixed surface point charges and a layered structure of counter ions (corresponding to Br$^-$ ions here) near the 'hard' surface was observed [32]. The details of the distribution of solvent/ions around colloidal particles can have significant effects on their dynamics [36]. Our present model can provide a more realistic description of the interfacial structure of CTAB-stabilised AuNRs and therefore their dynamic properties.

The plots of $acc.\rho_s$ *vs.* z in Figure 5 show how CTA$^+$ chains distribute in the inner/outer sub-layers in the systems. The

ligand surface density ρ_s in each sub-layer is also given. Interestingly, we can see that except at $\overline{\rho_s} = 1.5\,\mathrm{nm}^{-2}$ and $D_0 = 0.5$, where the boundary between inner/outer sub-layers is not clear, the CTA^+ chains are not equally distributed in the two sub-layers, with more ligands in the inner sub-layer than in the outer sub-layer especially at larger D_0^*. This contrasts to the equal distribution shown in Figure 4(b). These results indicate that when CTAB adsorbs on gold, the two sub-layers might be asymmetric, and thus the real surface charge density of a CTAB-stabilised AuNR could be lower than the average ρ_s estimated from the amount of adsorbed CTAB molecules. This effect could be another contribution to the discrepancy between surface charge densities estimated from the zeta potential and the ligand packing density [32, 45, 46].

In the systems with $\overline{\rho_s} = 2.5\,\mathrm{nm}^{-2}$, the average of ρ_s in the inner/outer sub-layers gives the saturated adsorption amount of CTAB molecules on the gold surface ($\rho_s^{\mathrm{satd.}}$). Our simulation results show that $\rho_s^{\mathrm{satd.}}$ increases as D_0^* increases (see Table 3). The values that we obtained are larger than the corresponding measure in the experiments (i.e. $\sim 1.8\,\mathrm{nm}^{-2}$ in >1 mM CTAB solutions [18]) even at $D_0^* = 0$ where we find that $\rho_s^{\mathrm{satd.}} \sim 2.0\,\mathrm{nm}^{-2}$. However, considering that the quantitative ability of DPD models is limited [37], especially for a system with electrolytes, our values of $\rho_s^{\mathrm{satd.}}$ are not bad.

The results above were obtained from simulations with CTAB molecules adsorbed on a [100] facet of an FCC solid made up of Au beads. As a coarse-grained model, we do not expect that our model will be as good as atomistic simulations in capturing the facet-dependent adsorption of CTAB molecules on different gold surfaces. However, for completeness, we compared the adsorption of CTAB on the [110] and [111] facets in systems with $\overline{\rho_s} = 2.0\,\mathrm{nm}^{-2}$ and $D_0^* = 1.0$. We observed compact CTAB bilayers with the same thickness forming and covering the whole gold surface in these simulations, with the only difference a slight decrease by ~2% of ρ_s for the inner sub-layer on the [110] facet due to its lower surface density of Au beads compared to that on the [100] and [111] facets in our model (see Figures 5 and 6). We did not observe the reduction of ρ_s for the inner sub-layer on [111] facets which was observed in the atomistic simulations [21, 22].

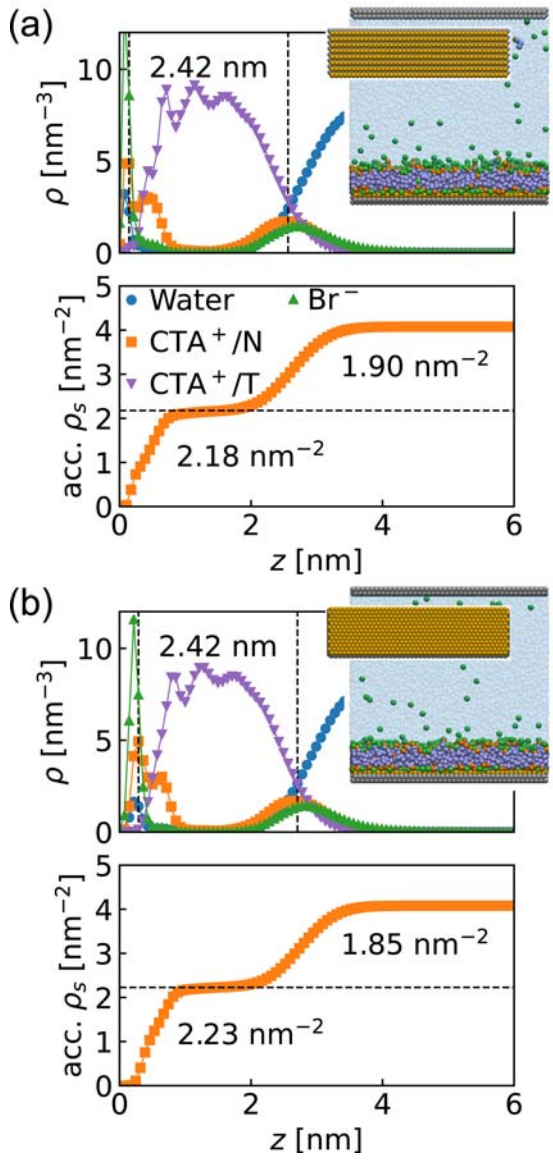

Figure 6. (Colour online) The density profiles (i.e. ρ *vs.* z) and the accumulative ρ_s along z (i.e. *acc.*ρ_s *vs.* z) for CTAB molecules on flat (a) [110] and (b) [111] gold surfaces in systems with $\overline{\rho_s} = 2.0\,\mathrm{nm}^{-2}$ and $D_0^* = 1.0$. The inserts show snapshots of the equilibrium configurations and the gold surfaces in these simulations.

3.2. CTAB molecules around a AuNR

Figure 7 shows snapshots of the equilibrium configurations for CTAB molecules around a AuNR obtained from simulations of systems with varying $\overline{\rho_s}$ and D_0. In the calculations of $\overline{\rho_s}$, considering the curvature effect, we use an offset of $\Delta = 1.2$ nm (i.e. approximate half of the thickness of the CTAB layer) to calculate the surface area using $A = [2L + \pi(d + 2\Delta)]L_y$. Due to the high CTAB concentration in the systems, CTAB molecules aggregated in all simulations.

At $D_0^* = 0$, CTAB molecules form free micelles even at $\overline{\rho_s} = 2.5\,\mathrm{nm}^{-2}$ (see Figure 7(a,f,k,p)), indicating an additional attraction is necessary to adsorb CTAB aggregates onto the small AuNR.

At $D_0^* = 0.5$, CTAB aggregates can be adsorbed on the surface of the AuNR but cannot wrap the whole AuNR even though there is a sufficient amount of CTAB for this to be possible (e.g. $\overline{\rho_s} = 2.0$ and $2.5\,\mathrm{nm}^{-2}$). The surface of the AuNR is therefore partially exposed to the aqueous solution (see Figure 7(b ,g,l,q)). Moreover, the CTAB aggregates preferentially adsorb at the sides of the AuNR, leaving the ends exposed.

At $D_0^* \geq 1.0$, similar configurations with exposed ends also form when there is not enough CTAB available (e.g. $\overline{\rho_s} \leq 1.5\,\mathrm{nm}^{-2}$, see Figure 7(c)–(e) and (h)–(j)). These configurations with no CTAB adsorbed on the ends provides support for the zipping-like growth mechanism [25, 47] for the anisotropic growth of AuNRs during the seeded growth synthesis. When there is a sufficient amount of CTAB available (e.g. $\overline{\rho_s} = 2.0$ and $2.5\,\mathrm{nm}^{-2}$), a compact CTAB bilayer forms and fully wraps the AuNR (see Figure 7(m)–(o) and (r)–(t)).

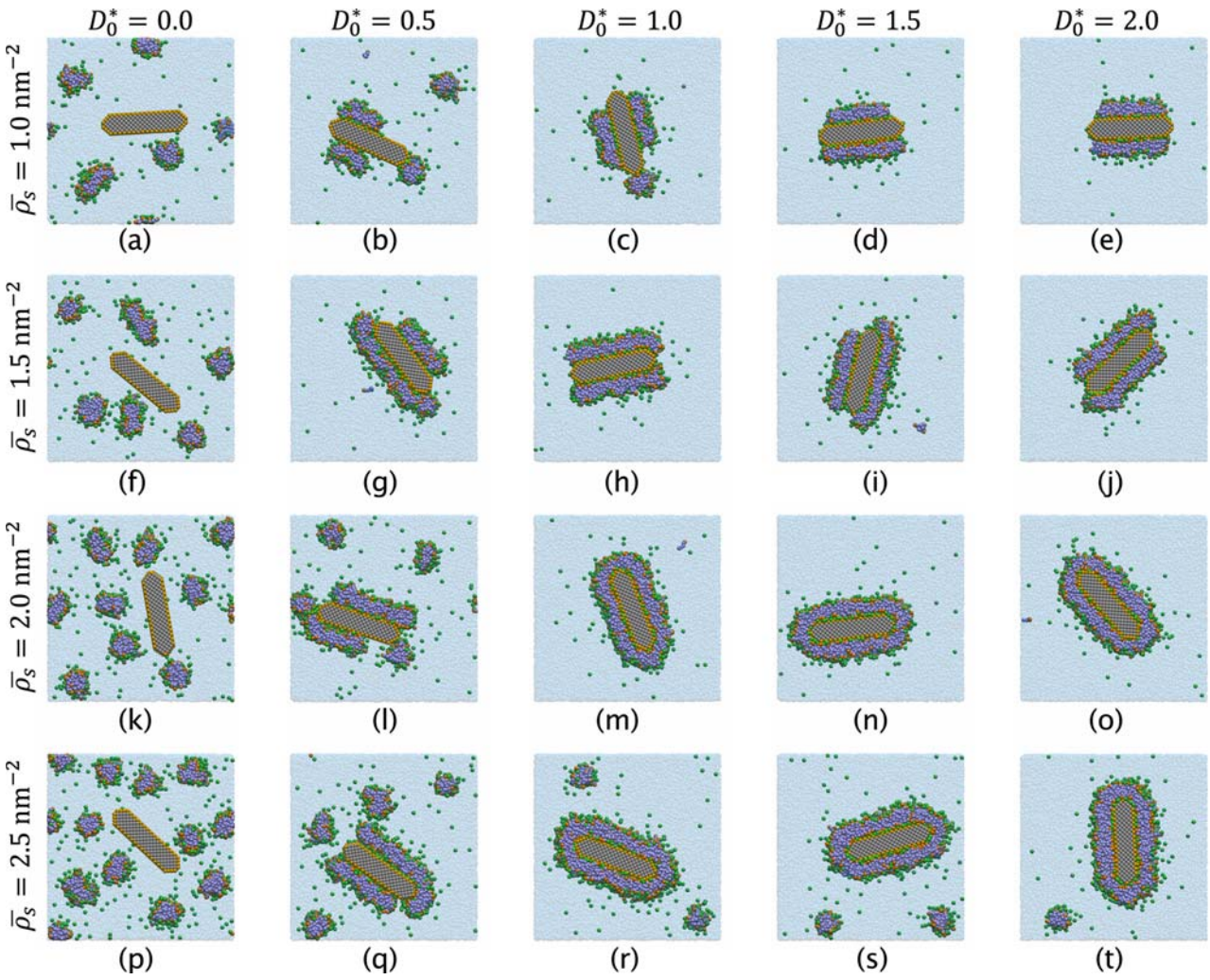

Figure 7. (Colour online) Snapshots of the equilibrium configurations for CTAB molecules around a AuNR obtained from simulations with different values of $\overline{\rho_s}$ and D_0.

The results above indicate that small AuNRs exhibit a significant end-effect for the adsorption of CTAB molecules. To further characterise this effect, we also analysed the local CTAB density along the AuNR surface in the systems that formed a compact CTAB bilayer (see Figure 8(a)). Figure 8 (b,c) shows the analysed results at $D_0^* = 1.0$ in the systems with $\overline{\rho_s} = 2.0$ and $2.5\ \mathrm{nm}^{-2}$. We can see a significant reduction of the CTAB density at the ends compared to that at the sides, which is similar to that observed in experiments for AuNRs with the diameter of ~15 nm [20]. Moreover, our simulations show this anisotropic distribution of CTAB molecules around the AuNR is more significant in the inner sub-layer and is much smaller in the outer sub-layer (e.g. $\overline{\rho_s} = 2.0\ \mathrm{nm}^{-2}$, see Figure 8(b)), with almost no reduction in the outer sub-layer at the saturated adsorption state (e.g. $\overline{\rho_s} = 2.5\ \mathrm{nm}^{-2}$, see Figure 8(c)).

Note that in our model, the ends of the AuNRs consist of small [110] and [100] facets (see Figure 2(b)). Our simulation results on the flat gold surface show only a weak facet-depended CTAB adsorption (see Figure 6) and thus the end-effect observed in our simulations with the small AuNR should be mainly caused by the high curvature of the ends. This is consistent with recent atomistic simulations [23].

4. Conclusions

In this work, we have developed a coarse-grained model based on the DPD method that can be used to study the adsorption of CTAB molecules on gold surfaces: the water and Br^- ions are modelled as conventional neutral W and charged Br beads, respectively; the CTA^+ chains are modelled as one charged N bead and four neutral T beads connected by bonds [37], and the solid gold is represented by a FCC crystal made up of Au beads (see Figures 1 and 2). We introduced a Au-Br^- attraction given by the Morse potential between Au and Br beads to mimic the electrostatic interaction between the cationic head groups of CTA^+ chains and Br^- ions adsorbed on the gold surface [24]. The organisation of CTAB molecules on flat gold surfaces and around a AuNR were studied using this model.

Overall, the proposed model with a proper Au-Br^- attraction (i.e. $D_0^* \leq 1.5$) can well reproduce the quantitative features of CTAB molecules adsorbed on flat gold surfaces that have been observed experimentally (e.g. the thickness of the CTAB layer [19] and the average ligand surface density [18]) at the saturated adsorption state. With an increase in the Au-Br^- attraction and the amount of CTAB in the system,

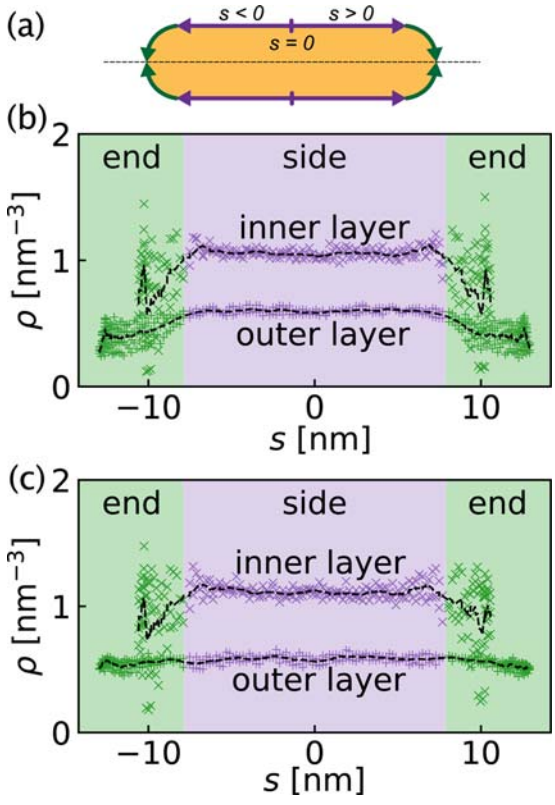

Figure 8. (Colour online) (a) Schematic illustration showing how we analysed the local density of CTAB molecules along the surface of the AuNR. *s* represents the distance from the centre of the side along the surface. The results are averaged over the top and bottom halves of the AuNR. (b)–(c) The local density (ρ) of N beads as a function of *s* near the density peaks in the inner/outer sub-layers at $D_0^* = 1.0$ in the systems with (b) $\overline{\rho_s} = 2.0\,\mathrm{nm}^{-2}$ and (c) $\overline{\rho_s} = 2.5\,\mathrm{nm}^{-2}$. The dash lines show the Savitsky-Golay filtered median of the scattered data.

the CTAB molecules change from being organised in micelles, to forming broken bilayers with channels, to forming compact bilayers. In particular, our simulations have revealed that in the CTAB bilayer, the inner layer bound on the gold surface can have a higher density than the outer layer exposed to the aqueous solution. This can result in AuNRs having a lower surface charge density than estimated from the average ligand surface density when assuming an equal distribution between the two layers.

For CTAB molecules on AuNRs, we found that a strong Au-Br^- attraction (i.e. $D_0^* \geq 1.0$) is needed to form a compact CTAB bilayer that fully wraps the small AuNR that we considered. Significantly, the CTAB aggregates preferentially adsorb at the sides of the AuNR. Thus, the ends of AuNRs are often exposed to the aqueous solution at small D_0^* or if there is an insufficient amount of CTAB molecules in the system. This provides support for the zipping-like growth mechanism that has been proposed to explain the anisotropic growth of AuNRs [25, 47]. This curvature-induced end-effect also leads to a reduction in the ligand density at the ends compared to that at the sides in the compact CTAB bilayer wrapping the whole AuNR.

Our model provides a fairly realistic description of the interfacial structure of CTAB-stabilised AuNRs, while being coarse-grained enough to allow for the study of entire nanoparticles. This should make it possible to simulate the dynamics of these AuNRs more accurately, especially to understand the role of CTAB molecules in self-assembly processes involving AuNRs [26–28] and in their phoretic motions [29–32].

Acknowledgments

The authors dedicate this work to Prof. Wenchuan Wang at Beijing University of Chemical Technology to celebrate his 80th birthday. This work was supported by the Australian Research Council under Grant CE170100026. Computational resources were provided by the Sydney Informatics Hub, a Core Research Facility of the University of Sydney.

Data Availability Statement

The data that support the findings of this study are available from the corresponding author upon reasonable request.

Disclosure statement

No potential conflict of interest was reported by the author(s).

Funding

This work was supported by the Australian Research Council [grant number CE170100026].

ORCID

Yawei Liu http://orcid.org/0000-0002-0230-0109
Jiachen Wei http://orcid.org/0000-0003-3802-5310
Daan Frenkel http://orcid.org/0000-0002-6362-2021
Asaph Widmer-Cooper http://orcid.org/0000-0001-5459-6960

References

[1] Perezjuste J, Pastorizasantos I, Lizmarzan L, et al. Gold nanorods: synthesis, characterization and applications. Coord Chem Rev. 2005;249:1870–1901. doi:10.1016/j.ccr.2005.01.030..
[2] Murphy CJ, Thompson LB, Alkilany AM, et al. The many faces of gold nanorods. J Phys Chem Lett. 2010;1:2867–2875. doi:10.1021/jz100992x..
[3] Chen H, Shao L, Li Q, et al. Gold nanorods and their plasmonic properties. Chem Soc Rev. 2013;42:2679–2724. doi:10.1039/C2CS35367A..
[4] Murphy CJ, Gole AM, Hunyadi SE, et al. Chemical sensing and imaging with metallic nanorods. Chem Commun. 2002;8:544–557. doi:10.1039/b711069c..
[5] Du Y, Jiang Q, Beziere N, et al. DNA-Nanostructure-Gold-Nanorod hybrids for enhanced in vivo optoacoustic imaging and photothermal therapy. Adv Mater. 2016;28:10000–10007. doi:10.1002/adma.201601710..
[6] Chang S, Li Q, Xiao X, et al. Enhancement of low energy sunlight harvesting in dye-sensitized solar cells using plasmonic gold nanorods. Energy Environ Sci. 2012;5:9444. doi:10.1039/c2ee22657j..
[7] Greybush NJ, Charipar K, Geldmeier JA, et al. Dynamic plasmonic pixels. ACS Nano. 2019;13:3875–3883. doi:10.1021/acsnano.9b00905.
[8] Pandey S, Thakur M, Mewada A, et al. Carbon dots functionalized gold nanorod mediated delivery of doxorubicin: tri-functional nano-worms for drug delivery, photothermal therapy and bioimaging. J Mater Chem B. 2013;1:4972. doi:10.1039/c3tb20761g.
[9] Funston AM, Novo C, Davis TJ, et al. Plasmon coupling of gold nanorods at short distances and in different geometries. Nano Lett. 2009;9:1651–1658. doi:10.1021/nl900034v.

[10] Thorkelsson K, Bai P, Xu T. Self-assembly and applications of anisotropic nanomaterials: a review. Nano Today. 2015;10:48–66. doi:10.1016/j.nantod.2014.12.005.
[11] Jana NR, Gearheart L, Murphy CJ. Wet chemical synthesis of high aspect ratio cylindrical gold nanorods. J Phys Chem B. 2001;105:4065–4067. doi:10.1021/jp0107964.
[12] Nikoobakht B, El-Sayed MA. Preparation and growth mechanism of gold nanorods (NRs) using seed-mediated growth method. Chem Mater. 2003;15:1957–1962.
[13] Busbee B, Obare S, Murphy C. An improved synthesis of high-aspect-ratio gold nanorods. Adv Mater. 2003;15:414–416. doi:10.1002/adma.200390095..
[14] Sau TK, Murphy CJ. Seeded high yield synthesis of short au nanorods in aqueous solution. Langmuir. 2004;20:6414–6420. doi:10.1021/la049463z.
[15] Lohse SE, Murphy CJ. The quest for shape control: a history of gold nanorod synthesis. Chem Mater. 2013;25:1250–1261. doi:10.1021/cm303708p.
[16] Nikoobakht B, El-Sayed MA. Evidence for bilayer assembly of cationic surfactants on the surface of gold nanorods. Langmuir. 2001;17:6368–6374. doi:10.1021/la010530o.
[17] Sau TK, Murphy CJ. Self-assembly patterns formed upon solvent evaporation of aqueous cetyltrimethylammonium bromide-coated gold nanoparticles of various shapes. Langmuir. 2005;21:2923–2929. doi:10.1021/la047488s.
[18] Kawasaki H, Nishimura K, Arakawa R. Influence of the counterions of cetyltrimetylammonium salts on the surfactant adsorption onto gold surfaces and the formation of gold nanoparticles. J Phys Chem C. 2007;111:2683–2690. doi:10.1021/jp066963n.
[19] Gómez-Graña S, Hubert F, Testard F, et al. Surfactant (Bi) layers on gold nanorods. Langmuir. 2012;28:1453–1459. doi:10.1021/la203451p.
[20] Janicek BE, Hinman JG, Hinman JJ, et al. Quantitative imaging of organic ligand density on anisotropic inorganic nanocrystals. Nano Lett. 2019;19:6308–6314. doi:10.1021/acs.nanolett.9b02434.
[21] Meena SK, Sulpizi M. Understanding the microscopic origin of gold nanoparticle anisotropic growth from molecular dynamics simulations. Langmuir. 2013;29:14954–14961. doi:10.1021/la403843n.
[22] Meena SK, Sulpizi M. From gold nanoseeds to nanorods: the microscopic origin of the anisotropic growth. Angew Chem Int Ed. 2016;55:11960–11964. doi:10.1002/anie.201604594.
[23] Da Silva JA, Netz PA, Meneghetti MR. Growth mechanism of gold nanorods: the effect of tip-surface curvature as revealed by molecular dynamics simulations. Langmuir. 2020;36:257–263. doi:10.1021/acs.langmuir.9b03235.
[24] Meena SK, Celiksoy S, Schäfer P, et al. The role of halide ions in the anisotropic growth of gold nanoparticles: a microscopic, atomistic perspective. Phys Chem Chem Phys. 2016;18:13246–13254. doi:10.1039/C6CP01076H.
[25] Da Silva JA, Meneghetti MR. New aspects of the gold nanorod formation mechanism via seed-mediated methods revealed by molecular dynamics simulations. Langmuir. 2018;34:366–375. doi:10.1021/acs.langmuir.7b03703.
[26] Anderson VJ, Lekkerkerker HNW. Insights into phase transition kinetics from colloid science. Nature. 2002;416:811–815. doi:10.1038/416811a.
[27] Boles MA, Engel M, Talapin DV. Self-assembly of colloidal nanocrystals: from intricate structures to functional materials. Chem Rev. 2016;116:11220–11289. doi:10.1021/acs.chemrev.6b00196.
[28] Lloyd JA, Liu Y, Ng SH, et al. Self-assembly of spherical and rod-shaped nanoparticles with full positional control. Nanoscale. 2019;11:22841–22848. doi:10.1039/C9NR06679A.
[29] Ahmed W, Kooij ES, Van Silfhout A, et al. Quantitative analysis of gold nanorod alignment after electric field-assisted deposition. Nano Lett. 2009;9:3786–3794. doi:10.1021/nl901968e.
[30] Tan Z, Yang M, Ripoll M. Anisotropic thermophoresis. Soft Matter. 2017;13:7283–7291. doi:10.1039/c7sm01436h.
[31] Wang Z, Niether D, Buitenhuis J, et al. Thermophoresis of a colloidal rod: contributions of charge and grafted polymers. Langmuir. 2019;35:1000–1007. doi:10.1021/acs.langmuir.8b03614.
[32] Zhang H, Liu Y, Shahidan MFS, et al. Direct assembly of vertically oriented, gold nanorod arrays. Adv Funct Mater. 2021;31:2006753. doi:10.1002/adfm.202006753.
[33] Praprotnik M, Site LD, Kremer K. Multiscale simulation of soft matter: from scale bridging to adaptive resolution. Annu Rev Phys Chem. 2008;59:545–571. doi:10.1146/annurev.physchem.59.032607.093707.
[34] Pagonabarraga I, Rotenberg B, Frenkel D. Recent advances in the modelling and simulation of electrokinetic effects: bridging the gap between atomistic and macroscopic descriptions. Phys Chem Chem Phys. 2010;12:9566. doi:10.1039/c004012f.
[35] Liu Y, Widmer-Cooper A. A versatile simulation method for studying phase behavior and dynamics in colloidal rod and rod-polymer suspensions. J Chem Phys. 2019;150:244508. doi:10.1063/1.5096193.
[36] Liu Y, Widmer-Cooper A. A dissipative particle dynamics model for studying dynamic phenomena in colloidal rod suspensions. J Chem Phys. 2021;154:104120. doi:10.1063/5.0041285.
[37] Mao R, Lee M-T, Vishnyakov A, et al. Modeling aggregation of ionic surfactants using a smeared charge approximation in dissipative particle dynamics simulations. J Phys Chem B. 2015;119:11673–11683. doi:10.1021/acs.jpcb.5b05630.
[38] Kremer K, Grest GS. Dynamics of entangled linear polymer melts: a molecular-dynamics simulation. J Chem Phys. 1990;92:5057–5086. doi:10.1063/1.458541.
[39] Groot RD, Warren PB. Dissipative particle dynamics: bridging the gap between atomistic and mesoscopic simulation. J Chem Phys. 1997;107:4423–4435. doi:10.1063/1.474784.
[40] Español P, Warren PB. Perspective: dissipative particle dynamics. J Chem Phys. 2017;146:150901. doi:10.1063/1.4979514.
[41] González-Melchor M, Mayoral E, Velázquez ME, et al. Electrostatic interactions in dissipative particle dynamics using the Ewald sums. J Chem Phys. 2006;125:224107. doi:10.1063/1.2400223.
[42] Plimpton S. Fast parallel algorithms for short-range molecular dynamics. J Comput Phys. 1995;117:1–19.
[43] Afrouzi HH, Farhadi M, Sedighi K, et al. Nano-colloid electrophoretic transport: fully explicit modelling via dissipative particle dynamics. Phys B Condens Matter. 2018;531:185–195. doi:10.1016/j.physb.2017.12.031.
[44] Li W, Zhang M, Zhang J, et al. Self-assembly of cetyl trimethylammonium bromide in ethanol-water mixtures. Front Chem China. 2006;1:438–442. doi:10.1007/s11458-006-0069-y.
[45] Kane V, Mulvaney P. Double-layer interactions between self-assembled monolayers of ω-mercaptoundecanoic acid on gold surfaces. Langmuir. 1998;14:3303–3311. doi:10.1021/la971296y.
[46] Kumal RR, Karam TE, Haber LH. Determination of the surface charge density of colloidal gold nanoparticles using second harmonic generation. J Phys Chem C. 2015;119:16200–16207. doi:10.1021/acs.jpcc.5b00568.
[47] Murphy CJ, Sau TK, Gole AM, et al. Anisotropic metal nanoparticles: synthesis, assembly, and optical applications. J Phys Chem B. 2005;109:13857–13870. doi:10.1021/jp0516846..